Holographic radius test plates for spherical surfaces with large radius of curvature

Quandou Wang, Ulf Griesmann,* and Johannes A. Soons

National Institute of Standards and Technology (NIST), Physical Measurement Laboratory, Semiconductor & Dimensional Metrology Division, Gaithersburg, Maryland 20899-8223, USA

*Corresponding author: ulf.griesmann@nist.gov

Received 8 April 2014; revised 23 May 2014; accepted 27 May 2014; posted 29 May 2014 (Doc. ID 209751); published 9 July 2014

We describe a novel interferometric method, based on nested Fresnel zone lenses or photon sieves, for testing and measuring the radius of curvature of precision spherical surfaces that have radii in a range between several meters and a few hundred meters. We illustrate the measurement concept with radius measurements of a spherical mirror with a radius of about 10 m. The measured radius is 9877 mm ± 10 mm for a coverage factor $k = 2$. Our measurements also demonstrate, for the first time to the best of our knowledge, the utility of photon sieves for precision surface metrology because they diffuse higher diffraction orders of computer generated holograms, which reduces coherent noise.

OCIS codes: (050.1965) Diffractive lenses; (220.4840) Testing.
http://dx.doi.org/10.1364/AO.53.004532

1. Introduction

Precise spherical surfaces are important for many applications in science and engineering. For example, spherical surfaces remain fundamental building blocks for even the most advanced optical imaging systems because spherical surfaces with low sphericity errors can be manufactured at acceptable cost [1]. Nearly spherical surfaces are characterized by the radius of the best-fit sphere, in the least squares sense, and the sphericity, a map of deviations from the best-fit sphere. The interferometric radius bench method is an established procedure for measuring the radius of curvature of convex or concave spherical surfaces when a low measurement uncertainty is required [2]. In this method a transmission sphere, or Fizeau objective, is used to create a spherical wavefront that comes to a focus. The spherical test surface is first positioned such that the focus is at the surface of the test part and the test beam of the interferometer is reversed (cat's eye position). The test part is then moved along the optical axis of the interferometer until its center of curvature coincides with the focus of the test beam (confocal position). The cat's eye and confocal positions can be located with low uncertainty using phase-shifting interferometry [3,4]. The distance between these two positions is the radius of the spherical test part. When a displacement measuring laser interferometer is used to measure the displacement between the cat's eye and confocal positions, relative uncertainties of 10^{-4} or below can be achieved [3,5,6]. Further improvement is possible when motion errors of the translation stage are characterized and compensated in the measurement [7,8]. In practice, the range of radii that can be measured with the radius bench method is limited by the length of the available radius bench. Larger radii can sometimes be measured using special setups in which the interferometer test beam is folded [9,10]. Generally, however, measurements of large radii with low uncertainty remain very challenging unless the radii are large enough to permit interferometric measurements against a transmission flat [11].

We have recently described a modified radius bench method for spherical test surfaces with large radius of curvature in which the transmission sphere is replaced by a nested zone lens that generates separate wavefronts for the cat's eye and

confocal positions [12]. The measurement procedure is illustrated in Fig. 1. A central zone lens creates a focus that defines a cat's eye position, while a larger annular zone lens is used to define a confocal position. In this way it becomes possible to measure a large radius using only a comparatively small displacement between the cat's eye and confocal positions, because

$$R = f_1 + f_2 + \delta, \tag{1}$$

where R is the radius of the spherical test part, f_1 and f_2 are the focal lengths of the annular and central zone lenses, and δ is the displacement between the cat's eye and confocal positions. Our first implementation of the nested zone lens successfully demonstrated the radius measurement method, but it had several disadvantages that limited its practical usefulness. The zone lenses were fabricated on a special wedged substrate with an angle between the front and back surfaces to eliminate interference between the surfaces. Wedged substrates are not only costly, but cause problems with the lithographic fabrication of the zone lenses because they are incompatible with most lithography tools. An even more serious problem is that the small diffraction angles in the zone lens for the confocal position make it very difficult to separate the diffraction orders of the zone lens. Even with a spatial filter in the imaging arm of the interferometer, the measurements were affected by a significant amount of coherent stray light from unwanted diffraction orders. In this paper we describe several improvements of the original concept described in [12] that overcome most of its limitations and make nested zone lenses a useful tool for characterizing the radii of spherical precision surfaces with a large radius of curvature.

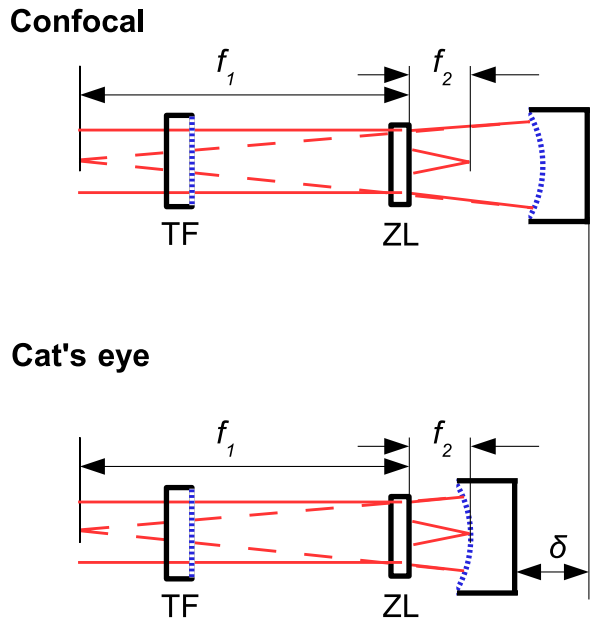

Fig. 1. Radius bench method with a nested zone lens (see [12]). ZL denotes the nested zone lens, and TF denotes an interferometer transmission flat. The surfaces of the interferometer cavity are indicated with dotted (blue) lines.

2. Measurement Setup

Instead of the radius bench setup described in [12] and shown in Fig. 1, in which the spherical test mirror is moved between the cat's eye and confocal positions, we chose the simplified measurement setup shown in Fig. 2. The zone lens (ZL in Fig. 2) is designed such that the cat's eye and confocal positions are the same. When the focus of the central zone lens with focal length, f_2, is on the test part surface, the curvature of the wavefront created by the annular zone lens matches the nominal curvature of the test part. This is equivalent to setting $\delta = 0$ in Eq. (1). The nested zone lens thus becomes a holographic test plate comparable to the interferometric test plates that are used in optics shops to test the radii of lens surfaces. When the focus of the central zone lens is located on the test part surface and no fringes are seen in the interferometer, the fringes observed in the annular area of the zone lens are a measure of the difference between the nominal and actual test part radius. The sensitivity of the annular fringe pattern to test part radius is low, allowing a relatively large range of test part radii to be measured with a single hologram while ultimately limiting the achievable accuracy of the method. For the design of the test plate an initial estimate of the part radius is required, which can be obtained, for example, with a mechanical spherometer.

Efficient lithographic fabrication of the nested zone lens at acceptable cost requires plane-parallel glass substrates. This, however, complicates the application of the zone lenses with interferometers because the reflection from the unpatterned substrate surface creates additional fringe systems that impede the analysis of the fringes originating from the test and reference surfaces that form the interferometer cavity of interest (indicated in blue curves in Figs. 1 and 2). This problem can be avoided by a design with a tilted zone lens, or a design in which the zone lens is set up in a focused test beam, as shown in Fig. 2, instead of a collimated beam. Our zone lenses were placed in the beam created by an f/7 transmission sphere (Fizeau objective) with an aperture of

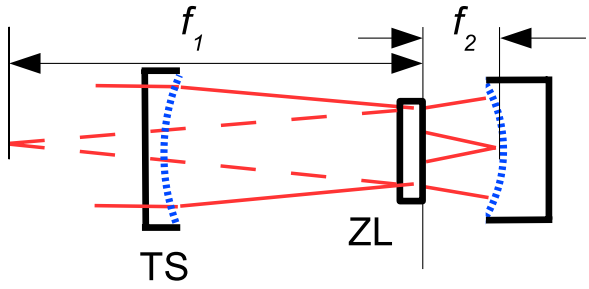

Fig. 2. Schematic of radius test setup with a holographic test plate. ZL denotes the nested zone lens, or photon sieve, and TS denotes an f/7 interferometer transmission sphere. The interferometer cavity is marked with dotted (blue) lines.

150 mm. A second important advantage of the noncollimated test beam is that the diffraction angles at the annular zone lens are increased, which makes it far easier to separate the diffraction orders of Fresnel type zone lenses.

We fabricated two types of holographic test plates for measuring the radius of an aluminum coated concave mirror with a radius of curvature of about 10 m and 50 mm part diameter. The respective zone lenses were positioned 350 mm from the intersection of the transmission sphere reference surface with the optical axis such that the zone lenses faced the test mirror. The central zone lens had a diameter of 10 mm and a focal length, f_2, of 80 mm. The annular zone lens had an outer diameter of about 50 mm, close to the diameter of the mirror under test, and a focal length of 9434 mm. The general layout of the zone lenses is shown in Fig. 3. An additional hologram is needed to align the test plate in the test beam of the interferometer [13]. The alignment hologram is the red annular area shown in Fig. 3. It is a Fresnel type retroreflector that was used in the 2nd diffraction order. The zone lenses were designed using commercial optical ray tracing software for a test mirror with a design radius of 9514 mm. The phase functions of the test plate zone lenses were modeled with radial Zernike polynomials; the phase function of the alignment retroreflector was modeled using an even radial polynomial. The phase functions of the zone lenses also compensate for the spherical aberration that is incurred by the focused test beam as it traverses the zone lens substrate.

Two types of test plates were fabricated. In the first type all holograms were realized as Fresnel type phase holograms. Fresnel zone boundaries were calculated from the phase functions using an isophase

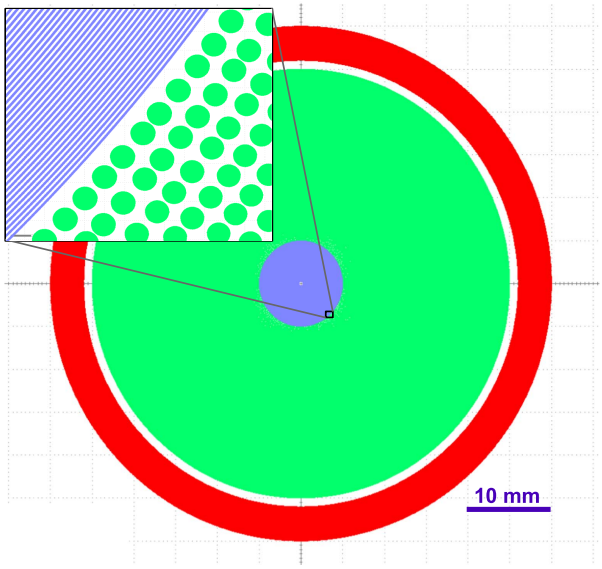

Fig. 3. Layout of a radius test plate with a central zone lens and an annular photon sieve. The red area (outer ring) is a Fresnel zone mirror that retroreflects the spherical test wavefront, for alignment of the hologram in the test beam of the interferometer.

contouring algorithm similar to the one described in [14]. Fresnel zone boundaries were then rendered with polygons suitable for lithographic fabrication using a maskless lithography tool. In the second type of test plate, the annular lens (green, largest shaded area, in Fig. 3) was realized as a phase photon sieve. Photon sieves were first suggested as improvements of Fresnel zone lenses and mirrors for the focusing of x rays [15–17]. They are related to earlier work on binary Gabor zone lenses [18] and on modulated zone lenses [19]. Photon sieves are derived from Fresnel zone lenses by replacing the contiguous Fresnel zones with circular apertures that are placed at randomized positions along the Fresnel zone. The distribution of aperture positions and the distribution of aperture diameters can be varied to tailor the optical properties of a photon sieve to a specific application. The greatest appeal of photon sieves for surface metrology applications, like the one described here, is that they offer a new approach to the management of diffraction orders. Fresnel zone lenses diffract light into higher diffraction orders at a discrete set of diffraction angles. With photon sieves it is possible to distribute the energy in the higher diffraction orders into a wide range of diffraction angles, because they consist of a large number of apertures at randomized angular positions. This makes it possible to reduce or eliminate coherent noise in interferometric surface form measurements. The inset in Fig. 3 shows a small section of the photon sieve layout that we designed for the radius test plate. Our design essentially follows the original photon sieve design introduced by Kipp *et al.* [15,16], without the radial apodization in aperture density to maintain uniform diffraction efficiency. For each Fresnel zone, the diameter of the photon sieve apertures was set to 1.53 times the width of the underlying zone. The azimuthal position of the apertures was randomized while overlapping apertures were avoided. The sum of the aperture areas belonging to a Fresnel zone was designed to be the same as the area of the underlying Fresnel zone. The aperture diameter was slightly adjusted to ensure an integral number of apertures. The central and alignment zone lenses were of the Fresnel type in both cases because the larger diffraction angle makes the separation of diffraction orders unproblematic.

The holographic radius test plates were fabricated in the Nano-Structured Optics Laboratory at the National Institute of Standards and Technology (NIST) on 6.5 mm thick substrates made from a borosilicate float glass [20] using a zone plate array lithography (ZPAL) tool [21,22]. During the lithographic exposure the temperature in the lithography tool was maintained at 20°C within 0.01°C. After patterning of the photoresist the substrates were dry etched in an argon–chlorine plasma to a depth $d = \lambda/(2n - 2) \approx 670$ nm, where $\lambda = 632.82$ nm is the laser wavelength, and $n = 1.47$ is the refractive index of the substrate material [23]. The etch depth was chosen to maximize the diffraction efficiency into

the ±1 diffraction orders. The alignment zone mirror (see Fig. 3) was used in the first diffraction order. During dry etching, the alignment zones were covered with an adhesive polyimide film after an etch depth of $d = \lambda/(4n) \approx 108$ nm was reached to ensure adequate diffraction efficiency for the alignment hologram [23].

3. Measurement Results and Uncertainty

Measurements of the spherical mirror with a nominal radius of 9514 mm were set up in the test beam of a phase-shifting Fizeau interferometer at NIST, which was equipped with an f/7 transmission sphere as indicated in Fig. 2. The holographic test plate was mounted in a 5-axis mount and aligned in the test beam such that a null fringe was obtained within the area of the retroreflecting alignment hologram. The test mirror was then positioned near the focus f_2 of the central zone lens. Figure 4 shows the interference fringes at the interferometer camera for the Fresnel type zone lens and for the photon sieve at approximately the same position inside the focus of the central zone lens. One clearly evident difference in the fringes is a much lower level of coherent high-frequency noise in the photon sieve fringes. Stray light from higher diffraction orders causes high-frequency fringes throughout the aperture in the Fresnel lens image (left image in Fig. 4). The level of coherent noise is significantly lower in the photon sieve images because the energy in the higher diffraction orders is diffused into a wide range of angles by the photon sieve instead of being concentrated at a few angles. The photon sieve has effectively only two diffracted wavefronts of orders +1 and −1. The image on the right in Fig. 4 also shows a high frequency error in the top quarter of the image that was traced to a misalignment of the lithography tool on the day the test plate was fabricated. It is of little consequence for the present application because we are exclusively interested in rotationally invariant properties of the zone lenses, which are not affected by the small lithography tool write error. The geometric errors of the two orthogonal linear air slides that form the motion system of the lithography tool are unlikely to cause a significant power error in the zone lenses. Thermal effects and errors due to errors in the scales of the lithography motion system are thought to be insignificant. A relative scale error in the zone lens pattern causes a relative error in the focal length of approximately twice the magnitude. The zone lenses were fabricated and used in temperature controlled laboratory spaces at a temperature of 20°C ± 0.02°C.

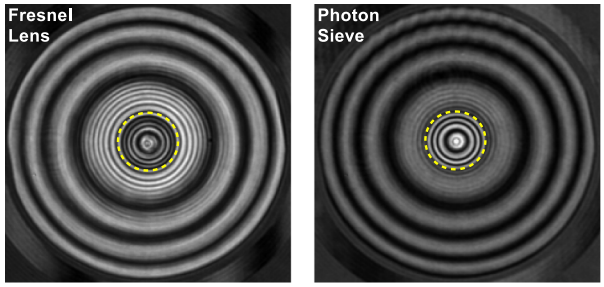

Fig. 4. Interferometer fringes of the interferometer cavity in Fig. 2 with a Fresnel type zone lens (left) and a photon sieve (right). The dashed (yellow) lines indicate the boundaries between the central and annular zone lenses.

The radius of the test mirror can be calculated from a measurement of the (spherical) defocus error term in the area of the annular zone lens. Figure 5 shows the test part surface and the reference wavefront when the test part is positioned *near the focus* of the central zone lens. The distance, d, measured by the interferometer is approximated by

$$d(\theta) \approx R + \Delta R - (\Delta R + \Delta z)\cos\theta, \tag{2}$$

where R is the nominal (design) radius of the mirror, ΔR is the radius error that we seek to measure, and Δz is the displacement of the test mirror's nominal center of curvature from the focal point of the outer zone lens, which, e.g., can be due to a position error of the test mirror at the confocal position (see also [24]). An interferometer with the measurement setup in Fig. 2 measures the difference, $\Delta m(\theta)$, between the test mirror surface and the test wavefront,

$$\begin{aligned}\Delta m(\theta) &= R - d(\theta)\\ &= -\Delta R + (\Delta R + \Delta z)\cos\theta\\ &\approx \Delta z - (\Delta R + \Delta z)\cdot\frac{1}{2}\theta^2.\end{aligned} \tag{3}$$

When δm is described with a defocus Zernike polynomial term, a_2^0,

$$\delta m = 2a_2^0\left(\frac{y}{r_a}\right)^2, \tag{4}$$

where r_a is the aperture radius on the test mirror, and $\theta \approx y/R$ for small angles, it follows that

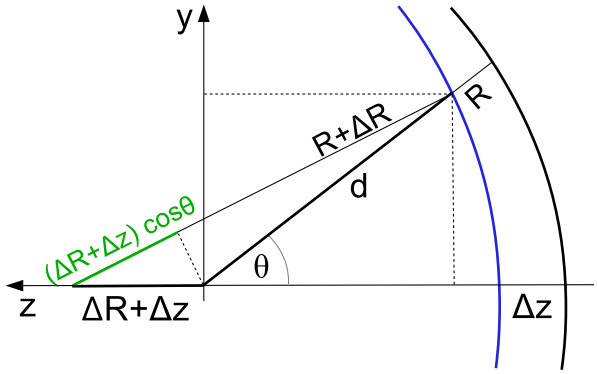

Fig. 5. Difference of test mirror surface (blue, left, arc) with design radius, R, and radius error, ΔR, and reference wavefront with design radius, R, (black, right, arc) when the mirror is positioned near the primary focus of the central zone lens with a displacement, Δz.

$$\Delta R + \Delta z = -4a_2^0\left(\frac{R}{r_a}\right)^2. \quad (5)$$

When the test part is positioned at the focus of the inner zone lens, $\Delta z = 0$ and the radius error, ΔR, of a mirror with nominal (design) radius, R, can be calculated from measurements of the defocus Zernike term, a_2^0, and the aperture radius, r_a, on the test mirror.

Five measurements of the wavefront within the central zone lens and the annular zone lens were made for several axial displacements around the focus of the central zone lens. Phase measurements were made by mechanical shifting of the test part using a phase-shifting algorithm with 7 samples and $\pi/2$ phase steps [25]. The wavefront error map in the central and annular areas was measured separately by masking either the central or annular zone lens. The Zernike defocus terms, a_2^0, in both areas were then calculated by fitting a Zernike polynomial consisting of constant, tilt, and defocus terms to the data. Figures 6 and 7 show the defocus terms in the annular areas as a function of the defocus term in the central zone lens areas for both the Fresnel (Fig. 6) and photon sieve (Fig. 7) test plates. Each data point, shown in red, represents the mean of five measurements, and the error bars indicate the standard deviation of the five measurements. They are a measure of the repeatability of the defocus terms. The error bars in horizontal direction are too small to be visible in Figs. 6 and 7. A straight line was fitted to the data sets for the Fresnel zone lens and the photon sieve to determine the defocus in the annular lens when the test mirror is positioned at the focus of the central zone lens. We applied an iterative, weighted, least squares fitting procedure to accommodate the large variation in the measurement repeatability of the annular defocus terms, especially in the case of the Fresnel zone lens measurements shown in Fig. 6. The weights equal the reciprocal of the noise variance of the mean defocus term at each position, modeled as the sum of the respective

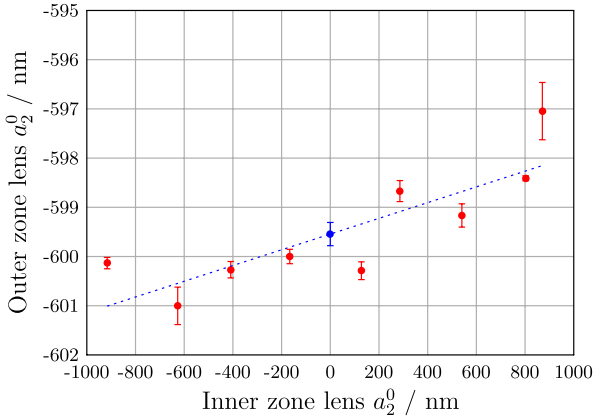

Fig. 6. Measured defocus Zernike coefficient in the outer zone lens (red circles, nonzero inner ZLs area) as functions of the defocus Zernike coefficient in the inner zone lens area.

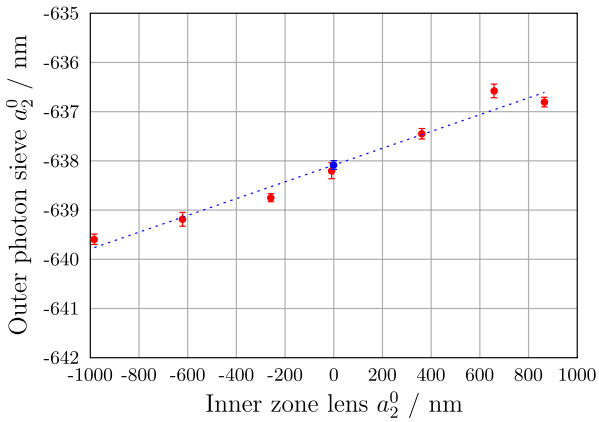

Fig. 7. Measured defocus Zernike coefficient in the outer photon sieve (red circles, nonzero inner ZLs area) as functions of the defocus Zernike coefficient in the inner zone lens area.

repeatability variance and the variance of other errors. The latter variance, assumed to be constant, was estimated from the difference between the observed and predicted variance of the residual errors after fitting. The blue circles in Figs. 6 and 7 indicate the values for the defocus of the annular lens *at* the focus (0 inner ZLs area) of the central zone lens and their estimated standard deviation. The radius of the test mirror was then calculated using Eq. (5) (for $\Delta z = 0$), from the defocus, a_2^0, and the design radius, $R = 9514$ mm. The diameter of the reflective mirror area, $2r_a$, measured with calipers, was 49.4 mm with a standard uncertainty of 0.12 mm.

Two sets of measurements—labeled A and B in the following—of the test mirror with both the Fresnel type zone lens and the photon sieve made several months apart. In both instances the experiment was set up and aligned from the beginning. The results of the measurements are summarized in Table 1. The table lists the aperture radius, r_a, in the second column. The third column lists the Zernike defocus term, a_2^0, of the annular zone lens at the focus of the inner zone lens, followed by the resulting radius error calculated using Eq. (5), in column four. The right column in Table 1 contains the estimates of the test mirror radius and their uncertainties. The difference in the annular zone lens defocus term of the Fresnel zone lens and the photon sieve was caused primarily by the differences in the curvature of the zone lens substrates. A quadratic (power) flatness error in the substrate causes

Table 1. Results of Two Radius Measurements of a Test Mirror With a Fresnel Type Nested Zone Lens (ZL) and a Nested Photon Sieve (PS)[a]

	r_a/mm	a_2^0/nm	ΔR/mm	$(R + \Delta R)$/mm
ZL A	24.7 ± 0.14	-603.1 ± 0.2	363.0 ± 4.1	9877 ± 5
ZL B	24.7 ± 0.14	-599.5 ± 0.2	360.9 ± 4.0	9875 ± 5
PS A	24.7 ± 0.14	-641.2 ± 0.1	364.7 ± 4.3	9879 ± 5
PS B	24.7 ± 0.14	-638.1 ± 0.1	362.8 ± 4.3	9876 ± 5

[a]Measured defocus values for the repeat measurements (B) are shown in Figs. 6 and 7

a position error of the hologram when it is aligned in the test beam using the annular alignment zone lens in reflection (see Fig. 3). This, in turn, results in a radius error of the test wavefront. The flatness errors of the substrates were measured and the radii, $R + \Delta R$ in Table 1, are corrected for the effect of the quadratic component in the substrate flatness error.

Calculating the spherical mirror radius with Eq. (5) requires an estimate of the aperture radius, r_a, in the interferogram, which corresponds to the unit circle radius for the calculation of the Zernike defocus term, a_2^0. In our case, the test beam overfilled the test mirror, which has a radius of 24.7 mm with a standard uncertainty of 0.12 mm. Precise measurement of the diameter of the reflective area of the test mirror in the interferograms was difficult, resulting in a standard uncertainty of 0.9 camera pixels, which, for our measurement setup, corresponds to a standard uncertainty for the aperture radius uncertainty of 64 μm. The combined standard uncertainty, $u(r_a)$, for the aperture radius at the Zernike normalization radius is, thus, 0.14 mm.

The uncertainty of the radius error, ΔR, is calculated from the uncertainty, $u(a_2^0)$, of the Zernike defocus coefficient, and the uncertainty, $u(r_a)$, of the aperture radius r_a, using the familiar error propagation formula for uncorrelated variables [26],

$$u(\Delta R) = 4\left(\frac{R}{r_a}\right)^2 \sqrt{u(a_2^0)^2 + 4\left(\frac{a_2^0}{r_a}\right)^2 u(r_a)^2}. \quad (6)$$

The defocus coefficients, a_2^0, for the annular zone lenses were estimated using a set of defocus measurements near the focus of the central zone lens as shown in Figs. 6 and 7. The defocus coefficients and their standard deviation *at* the focus of the central zone lens were estimated using a straight line fit. The resulting uncertainties for the radius errors in our measurements are listed in Table 1.

There are additional sources of uncertainty. Good alignment with less than one fringe visible in the area of the alignment hologram was difficult with the available mount for the zone lens. We estimate that we were able to achieve an alignment error in the direction of the optical axis of no more than 10 μm. This results in an additional uncertainty for the radius error of about 1 mm. This uncertainty was added, in quadrature, to the uncertainty of the radius errors, ΔR, shown in Table 1 to calculate the uncertainty of the mirror radii, $R + \Delta R$, which are shown in the last column of Table 1. The effects of write errors of the lithography tool were estimated to be negligible. Intuitively this can be understood by realizing that a scale error, β, in a zone lens pattern causes an error of approximately $2f\beta$ in its focal length, f [27]. In our case, β is on the order of several μm per m. The zone lenses were designed for a nominal substrate thickness of 6.5 mm. The actual thicknesses of the two substrates differed from the nominal thickness by about 200 μm. The resulting change in the measured radius error is, however, insignificant as the alignment hologram compensates most of the resulting power error in the test beam.

It is instructive to examine Eq. (6) for the uncertainty of the radius that follows from Eq. (5) when the effects of errors in the hologram and its alignment are ignored. It turns out that the uncertainty of the radius is dominated by the uncertainty, $u(r_a)$, of the aperture radius, r_a. This is largely a consequence of the large radius error, ΔR, of the test mirror, resulting in a large value for a_2^0, and our zone lens design, which slightly overfilled the test mirror. A better zone lens design would underfill the test mirror. The aperture radius can then be calculated from the optical design and its uncertainty only depends on the uncertainty inherent in the zone lens fabrication and the estimate of the pixel radius corresponding to the aperture radius. Alternatively, fiducials on the mirror could be used to obtain a better estimation of the mirror diameter. A low uncertainty for the aperture radius, $u(r_a)$, is important, especially when the actual mirror radius differs appreciably from the design radius because of the increasing weight, $(2a_2^0/r_a)^2$, in Eq. (6).

When a lower measurement uncertainty is required, it may be preferable to measure ΔR directly by measuring the distance between the cat's eye position for the central zone lens and the confocal position for the annular zone lens using a displacement measuring laser interferometer similar to the measurement procedure described in [12,27]. This removes the errors resulting from measuring the outer zone lens in a non-null configuration, eliminates errors due to the uncertainty in the effective aperture radius, r_a, and increases the sensitivity (resolution) of the radius error measurements.

4. Summary and Conclusion

We have demonstrated a new method for measuring the radius of precision spherical surfaces with large radius based on a pair of nested zone lenses or photon sieves that are fabricated on a flat substrate. The relative standard uncertainty of about 5×10^{-4} is comparable to the uncertainty that is typically achieved with the radius bench method for shorter radii. Improved uncertainties can be achieved for parts with a smaller radius error, or when the distance between the cat's eye and confocal positions is measured with a displacement measuring laser interferometer, as described in [12,27]. The incorporation of nonlinear effects in the interpretation of the annular zone lens defocus can also reduce the measurement errors when the actual radius of the test mirror significantly deviates from the design value. Our measurement was the first, to the best of our knowledge, to apply a photon sieve in solving a measurement problem in precision surface metrology. Our measurements show that the photon sieve enabled us to manage diffraction orders of a binary diffractive optic in a situation where unwanted diffraction orders

would otherwise be difficult to filter out. The reduction in coherent noise is evident in the interferograms in Fig. 4 and the reduced uncertainties in Fig. 7. This result is, potentially, of broader significance for the application of diffractive optics as null correctors in interferometric precision metrology. The design of diffractive null correctors is often complicated by the need to filter out light from unwanted diffraction orders. Photon sieves appear to offer a new way to manage stray light from higher diffraction orders.

Our research was in part performed using resources provided by the NanoFab of the NIST Center for Nanoscale Science and Technology.

References

1. F. Twyman, *Prism and LensMaking: A Textbook for Optical Glassworkers*, 2nd ed. (CRC Press, 1988).
2. J. E. Greivenkamp and J. H. Bruning, "Phase shifting interferometry," in *Optical Shop Testing*, D. Malacara, ed., 2nd ed. (Wiley, 1992), pp. 574–580.
3. L. Selberg, "Radius measurement by interferometry," Opt. Eng. **31**, 1961–1966 (1992).
4. U. Griesmann, J. Soons, and Q. Wang, "Measuring form and radius of spheres with interferometry," CIRP Ann. **53**, 451–454 (2004).
5. T. L. Schmitz, A. D. Davies, and C. J. Evans, "Uncertainties in interferometric measurements of radius of curvature," Proc. SPIE **4451**, 432–447 (2001).
6. T. L. Schmitz, C. J. Evans, A. Davies, and W. T. Estler, "Displacement uncertainty in interferometric radius measurements," CIRP Ann. **51**, 451–454 (2002).
7. A. Davies and T. L. Schmitz, "Correction for stage error motions in radius measurements," Appl. Opt. **44**, 5884–5893 (2005).
8. T. L. Schmitz, N. Gardner, M. Vaughn, K. Medicus, and A. Davies, "Improving optical bench radius measurements using stage error motion data," Appl. Opt. **47**, 6692–6700 (2008).
9. M. C. Gerchman and G. C. Hunter, "Differential technique for accurately measuring the radius of long radius concave optical surfaces," Opt. Eng. **19**, 843–848 (1980).
10. K. Freischlad, M. Küchel, W. Wiedmann, W. Kaiser, and M. Mayer, "High precision interferometric testing of spherical mirrors with long radius of curvature," Proc. SPIE **1332**, 8–17 (1990).
11. R. E. Parks, C. J. Evans, P. J. Sullivan, L.-Z. Shao, and B. Loucks, "Measurements of the LIGO pathfinder optics," Proc. SPIE **3134**, 95–111 (1997).
12. Q. Wang, G. Gao, and U. Griesmann, "Radius measurement of spherical surfaces with large radii-of-curvature using dual-focus zone plates," in *Optical Fabrication and Testing (OF&T)* (Optical Society of America, 2008), paper OWB2.
13. A. F. Fercher and M. Kriese, "Justierung synthetischer Hologramme mit kugelförmigen Referenzwellen (engl.: Alignment of synthetic holograms with spherical reference waves)," Optik **36**, 547–551 (1972).
14. B. Kress and P. Meyrueis, *Digital Diffractive Optics* (Wiley, 2000).
15. L. Kipp, M. Skibowski, R. L. Johnson, R. Bernd, R. Adelung, S. Harm, and R. Seemann, "Sharper images by focusing soft x-rays with photon sieves," Nature **414**, 184–188 (2001).
16. Q. Cao and J. Jahns, "Focusing analysis of the pinhole photon sieve: individual far-field model," J. Opt. Soc. Am. A **19**, 2387–2393 (2002).
17. J. Jahns, Q. Cao, and S. Sinziger, "Micro- and nanooptics—an overview," Laser Photon. Rev. **2**, 249–263 (2008).
18. T. D. Beynon, I. Kirk, and T. R. Mathews, "Gabor zone plate with binary transmittance values," Opt. Lett. **17**, 544–546 (1992).
19. A. Engel and G. Herziger, "Computer-drawn modulated zone plates," Appl. Opt. **12**, 471–479 (1973).
20. Q. Wang and U. Griesmann, "A versatile bilayer resist for laser lithography at 405 nm on glass substrates," Opt. Eng. **52**, 105104 (2013).
21. H. I. Smith, M. E. Walsh, F. Zhang, J. Ferrera, G. Hourihan, D. Smith, R. Light, and M. Jaspan, "An innovative tool for fabricating computer-generated holograms," J. Phys. Conf. Ser. **415**, 012037 (2013).
22. R. Menon, A. Patel, D. Chao, M. Walsh, and H. I. Smith, "Zone-plate-array lithography (ZPAL): optical maskless lithography for cost-effective patterning," Proc. SPIE **5751**, 330–339 (2005).
23. D. C. O'Shea, T. J. Suleski, A. D. Kathman, and D. W. Prather, *Diffractive Optics: Design, Fabrication, and Test* (SPIE, 2004).
24. W. J. Smith, *Modern Optical Engineering*, 2nd ed. (McGraw-Hill, 1990), pp. 328–329.
25. P. de Groot, "Derivation of algorithms for phase-shifting interferometry using the concept of a data-sampling window," Appl. Opt. **34**, 4723–4730 (1995).
26. H. H. Ku, "Notes on the use of propagation of error formulas," J. Res. Natl. Bur. Stand. **70C**, 263–273 (1966).
27. Q. Wang, J. A. Soons, and U. Griesmann, "Holographic radius test plates," Proc. SPIE **8838**, 88380I (2013).